



Inverse measurement of wall pressure field in flexible-wall wind tunnels using global wall deformation data

Kenneth Brown^{1,2} · Julian Brown¹ · Mayuresh Patil¹ · William Devenport¹

Received: 25 March 2017 / Revised: 17 November 2017 / Accepted: 26 December 2017 / Published online: 15 January 2018
© Springer-Verlag GmbH Germany, part of Springer Nature 2018

Abstract

The Kevlar-wall anechoic wind tunnel offers great value to the aeroacoustics research community, affording the capability to make simultaneous aeroacoustic and aerodynamic measurements. While the aeroacoustic potential of the Kevlar-wall test section is already being leveraged, the aerodynamic capability of these test sections is still to be fully realized. The flexibility of the Kevlar walls suggests the possibility that the internal test section flow may be characterized by precisely measuring small deflections of the flexible walls. Treating the Kevlar fabric walls as tensioned membranes with known pre-tension and material properties, an inverse stress problem arises where the pressure distribution over the wall is sought as a function of the measured wall deflection. Experimental wall deformations produced by the wind loading of an airfoil model are measured using digital image correlation and subsequently projected onto polynomial basis functions which have been formulated to mitigate the impact of measurement noise based on a finite-element study. Inserting analytic derivatives of the basis functions into the equilibrium relations for a membrane, full-field pressure distributions across the Kevlar walls are computed. These inversely calculated pressures, after being validated against an independent measurement technique, can then be integrated along the length of the test section to give the sectional lift of the airfoil. Notably, these first-time results are achieved with a non-contact technique and in an anechoic environment.

1 Introduction

This section introduces the concept of the Kevlar-wall test section, provides motivation for measurements of the wall pressure field in such test sections, and describes the inverse nature of the pressure measurement.

1.1 Kevlar-wall test section

Since 2006, a new type of test section for aeroacoustic and aerodynamic testing has emerged using side walls which are formed from tensioned Kevlar fabric to serve as acoustic windows (Smith et al. 2005; Remillieux et al. 2008; Devenport et al. 2010, 2013; Brown 2016). The large rectangular openings in the side walls cover the full height and a large portion of the streamwise length of the test section and are

covered with Kevlar fabric. The test section is unique in that the tensioned fabric contains the freestream flow within the test section while allowing noise to pass outside where it can be measured by shielded acoustic instrumentation in anechoic chambers. It is this tensioned fabric with both limited flexibility and porosity which provides the aeroacoustic advantages of the Kevlar-wall test section yet presents unique challenges for aerodynamic instrumentation.

1.2 Motivation for novel measurements

One area of the Kevlar-wall system that is lacking is the compliment of instrumentation available for aerodynamic measurements. As demonstrated by Devenport et al. (2013) and Ito et al. (2010), Kevlar-wall test sections are capable of producing accurate aerodynamic data from airfoil pressure taps, wake rakes, and force-balances. Unlike in solid-wall test sections, however, there is of yet no reliable means to measure the wall pressures in a Kevlar-wall environment.

The wall pressure field is used in solid-wall test sections as an alternate means by which to measure lift produced by a model which is accomplished via a control volume analysis in the test section (Von Doenhoff and Abbott 1947). Lift

✉ Kenneth Brown
kenbrown@vt.edu

¹ Department of Aerospace and Ocean Engineering, Virginia Tech, Blacksburg, VA, USA

² Department of Mechanical Engineering, Virginia Tech, Blacksburg, VA, USA

measurements from wall pressures are favored in some wind tunnels as they permit the model to be free of static pressure taps, thus reducing the cost requirements for repeated instrumentation of individual models, as well as offering a non-intrusive technique with no potential for tap-induced tripping of the airfoil boundary layer. In facilities where model pressure taps are in fact present, wall pressure data additionally diagnose non-uniformities in the flow away from the model taps, as well as describe the test section flow when the model taps are unavailable due to simultaneous measurements by other instrumentation techniques such as in Joseph et al. (2016). Finally and importantly, engineers use wall pressures to correct for wall interference with the one-variable or two-variable methods when corrections based on linear theory are insufficient (Ashill et al. 1998). Given an accurate porosity model of the Kevlar fabric to account for the second variable, the potential for full-field wall pressure measurements afforded by a Kevlar sensing surface is particularly compatible with the two-variable method which requires a high density of pressure measurements at the wind tunnel boundaries (Ashill and Keating 1988).

It is thus desired to measure Kevlar-wall pressures primarily to provide an alternate means of measuring model lift, but also to aid in troubleshooting and correcting wind tunnel results. A preliminary approach is to mount small pressure taps on the non-flow side of the Kevlar walls which sense the pressures within the test section (Brown 2014; Brown et al. 2014). However, these taps are prone to leaking and become dislodged when the Kevlar is placed under high loading. An intriguing possibility is to instead employ the Kevlar itself as a sensing surface, in essence using the fabric as a full-field strain gauge to measure wind loading via the fluid–structure interaction with the walls.

1.3 Background of inverse problem

The proposed measurement using the Kevlar as a sensing surface constitutes an inverse problem of structural mechanics, since it requires determining a load from a deflection. Unlike the forward problem, the inverse problem does not necessarily depend continuously on the input data. Such a state of events follows naturally from the governing equilibrium equations in structural mechanics which involve derivatives of the displacement field on one side of the equation equated to the loads on the other side. The process of differentiation amplifies errors in a data set, so small errors in the input displacement field such as from measurement noise result in larger errors in the final solution of the loading (Stevens 1987).

To stabilize the solution, one can use a regularization technique such as by projecting displacement data onto a finite-dimensional model and solving for the loading that produces least-squares minimization with the measured data (Engl and

Kugler 2005; Vogel 2002). In the case of over-determined linear problems, the result is a minimization problem to find the optimal loading vector. The order of the finite-dimensional model must be carefully specified to damp out noise while not removing essential information about the character of the solution. Several authors have used such projection methods to solve inverse problems in the context of fluid–structure interaction problems as presented below.

Shkarayev et al. (2001) approaches the inverse problem seeking to reconstruct loads, stresses, and displacements from surface strain data such as on a wing of an aircraft. The loading distribution is formulated as a series of Chebyshev polynomials which provide the loading input to a linear finite-element model. The coefficients of the polynomials are varied and the surface strains calculated until the calculated strains match the measured strains in a least-squares sense.

Stanford et al. (2007) measure the deformation of a membrane wing with digital image correlation (DIC) and solve the inverse pressure problem using least-squares projection and a linear membrane formulation of finite elements. A set of polynomial functions ranging from third-order to sixth-order are employed as the basis functions, yet some of the inversely calculated pressure distributions have non-intuitive features that are presumably the result of over-fitting of experimental data with too many degrees of freedom.

Carpenter and Albertani (2013) also use DIC measurements to infer pressure distributions on a membrane wing using least-squares projection. The authors take a simpler approach than those above and simply project the out-of-plane strain data onto polynomial basis functions. Since the membrane deformation is geometrically non-linear, the authors use an empirical approximation to describe the small in-plane strain components. The end result is a polynomial representation of both strain and displacement that are used to directly evaluate the membrane equilibrium equation and produce a continuous pressure field.

This article works to solve a similar inverse fluid–structure interaction problem to that of Carpenter and Albertani as applied to the Kevlar walls of an aeroacoustic wind tunnel. The objective is the development of a technique to measure the full-field wall-boundary conditions in the wind tunnel. Below, the necessary theory of structural and fluid mechanics is reviewed, followed by the solution approach, the details of the wind tunnel setup, a sensitivity study of the inputs to the inverse problem, the validation results for the new instrumentation technique, and concluding remarks.

2 Theory/approach

This section details the theory of the structural mechanics of woven fabric, then describes the process for the regularization of noisy data as well as the fluid control volume calculations and the overall solution approach.

2.1 Continuum representation

Plain-woven fabrics such as the Kevlar used in this study consist of fibers running in perpendicular directions which permit openings, or pores, depending on the spacing between the fibers. While the strain field of a fabric cannot be considered continuous if the region of interest is only several pores in length, the continuum assumption may be valid if the non-uniformity of the deformation is small on the scales of the fiber pores (Hearle et al. 1980). The mathematical basis for applying a continuum model to woven fabrics or composites stems from perturbation analyses of the governing elasticity equations (Chung et al. 1999; Peng and Cao 2002). As ϵ , the ratio of the length of the periodic micro-scale in the fabric to the length-scale of the macroscopic fabric sheet, tends towards zero, the effect of the micro-scale geometry on the macro-scale is described by a set of effective material properties which can be determined through simulations on the micro-scale geometry or alternatively by experiment. The fabric used in this study has 13 pores per cm contained within a characteristic length over 1.85-m giving $\epsilon \approx 4e-4$ which is sufficiently small to suggest that the continuum model is valid.

Continuum behavior of the fabric is thus assumed, and specifically, the orthotropic elastic lamina is taken as a suitable continuum model for plain-woven fabric (Kilby 1963). The orthotropic designation refers to the fact that the two directions of the fibers correspond to two perpendicular planes of elastic symmetry. The elastic designation can be employed for fabrics when strains are small enough to permit linear approximations to the non-linear material properties and when hysteresis is negligible as should be the case for pre-conditioned fabrics (Beccarelli 2015). The lamina designation refers to the small thickness of the material which implies plane stress behavior. In fact, the thin cross-section of the Kevlar in this study yields a flexural rigidity of only 0.007 N/m. Given such low rigidity, both bending and twisting stresses are taken to be negligible, and the lamina may be more appropriately designated a membrane.

The continuum representation of a differential membrane element within a larger membrane sheet is shown in Fig. 1. The figure includes tension forces per unit length T_x , T_y , and T_{xy} , normal-acting pressure difference Δp , and thickness h . While the membrane's boundary conditions may be approximately taken as pinned in all three dimensions, this is an

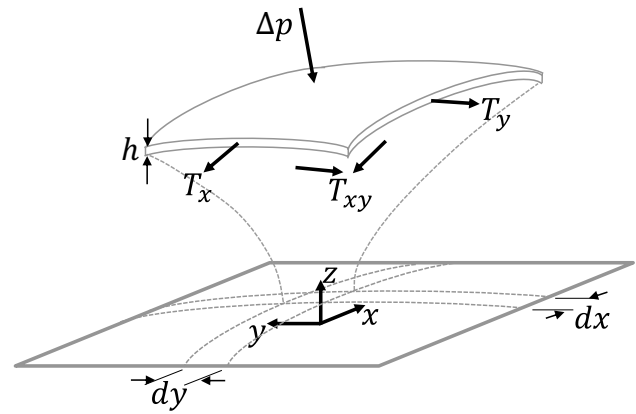


Fig. 1 Differential membrane element within a larger membrane sheet under load

approximation that is not strictly enforced in the wind tunnel experiments as will be explained further below.

2.2 Membrane mechanics

The strain–displacement relations for a membrane are given according to the following equations:

$$\epsilon_x = \frac{\partial u}{\partial x} + \frac{1}{2} \left(\frac{\partial w}{\partial x} \right)^2 \quad (1)$$

$$\epsilon_y = \frac{\partial v}{\partial y} + \frac{1}{2} \left(\frac{\partial w}{\partial y} \right)^2 \quad (2)$$

$$\gamma_{xy} = \frac{\partial u}{\partial y} + \frac{\partial v}{\partial x} + \frac{\partial w}{\partial x} \frac{\partial w}{\partial y}, \quad (3)$$

where ϵ_x , ϵ_y , and γ_{xy} are strains in the direction indicated by their subscripts, and u , v , and w are the displacements in the x -, y -, and z -directions, respectively (Timoshenko and Goodier 1970). These equations represent a geometrically non-linear membrane which has degrees of freedom in all three directions.

The relations between stress and strain for an orthotropic elastic membrane are given by the following equations:

$$T_{x,\epsilon} = \frac{E_x h}{1 - \nu_{xy} \nu_{yx}} (\epsilon_x + \nu_{yx} \epsilon_y) \quad (4)$$

$$T_{y,\epsilon} = \frac{E_y h}{1 - \nu_{xy} \nu_{yx}} (\epsilon_y + \nu_{xy} \epsilon_x) \quad (5)$$

$$T_{xy,\epsilon} = G h \gamma_{xy}, \quad (6)$$

where $T_{x,\varepsilon}$, $T_{y,\varepsilon}$, and $T_{xy,\varepsilon}$ are tensions in the direction indicated by their subscripts, E are elastic moduli, ν are Poisson's ratios, G is the shear modulus, h is the effective fabric thickness, and the ε subscript indicates the strain-induced tension as opposed to pre-tension (Timoshenko and Goodier 1970).

The out-of-plane equilibrium equation of a membrane gives the pressure difference across the membrane, Δp , as follows:

$$\Delta p = (T_{x,\varepsilon} + T_{x,0}) \frac{\partial^2 w}{\partial x^2} + (T_{y,\varepsilon} + T_{y,0}) \frac{\partial^2 w}{\partial y^2} + 2(T_{xy,\varepsilon} + T_{xy,0}) \frac{\partial^2 w}{\partial x \partial y}, \quad (7)$$

where the subscript 0 refers to the pre-tension as opposed to the strain-induced tension indicated by the subscript ε . The effects of gravity are here ignored as the weight per unit horizontal length of the Kevlar sheet is 1.1 N/m which is three orders of magnitude smaller than the pre-tension applied to the sheet. Equation 7 is geometrically non-linear as seen in the dependence of $T_{x,\varepsilon}$, $T_{y,\varepsilon}$, and $T_{xy,\varepsilon}$ on w . Proceeding now to insert Eqs. 1, 2, and 3 into Eqs. 4, 5, and 6, and substituting the results into Eq. 7, we have the following equation:

$$\Delta p = \left[\frac{E_x h \left[\frac{\partial u}{\partial x} + \frac{1}{2} \left(\frac{\partial w}{\partial x} \right)^2 + \nu_{yx} \left(\frac{\partial v}{\partial y} + \frac{1}{2} \left(\frac{\partial w}{\partial y} \right)^2 \right) \right]}{1 - \nu_{xy} \nu_{yx}} + T_{x,0} \right] \frac{\partial^2 w}{\partial x^2} + \left[\frac{E_y h \left[\frac{\partial v}{\partial y} + \frac{1}{2} \left(\frac{\partial w}{\partial y} \right)^2 + \nu_{xy} \left(\frac{\partial u}{\partial x} + \frac{1}{2} \left(\frac{\partial w}{\partial x} \right)^2 \right) \right]}{1 - \nu_{xy} \nu_{yx}} + T_{y,0} \right] \frac{\partial^2 w}{\partial y^2}, \quad (8)$$

where the shear terms have been neglected due to the small magnitude of the shear modulus as discussed in the following section. Note that any load-induced loss in pre-tension caused by imperfect pinning of the boundary conditions is accounted for, to the accuracy of the material model, by the inclusion of the measured $\frac{\partial u}{\partial x}$ and $\frac{\partial v}{\partial y}$ terms in Eq. 8.

2.3 Material properties

Using the relations of Eqs. 4, 5, and 6, the constitutive behavior of the Kevlar fabric is embodied by five parameters: E_x , E_y , ν_{xy} , ν_{yx} , and G . As symmetry dictates that $E_x \nu_{yx} = E_y \nu_{xy}$, one of the ν terms will be dependent on the other terms. Furthermore, G is effectively removed from the problem according to measurements of Kevlar fabric which show that the magnitude of the shear force is dwarfed by that of the tensile forces by three orders of magnitude in the absence of shear locking (Dong et al. 2010). While the shear force is thus taken to be negligible on a local level, it

should be borne in mind that this formulation is not rigorous on the global level, since an effective shear force is required if in-plane tensions are to vary throughout the membrane.

It is desired to know the functional form and value of the three remaining terms for the material properties: E_x , E_y , and ν_{xy} . Measurements on Kevlar fabric have shown varying degrees of non-linearity in the material properties, mainly as a consequence of crimp interaction between woven fibers (Dong et al. 2010; Zhu et al. 2013). The material model used in the present study is simplified to be linearly elastic, and the material properties are derived from measurements performed by the authors using an inflation test on a rectangular Kevlar sheet (Brown 2016). Though the experiment was set up to roughly match the state of strain experienced by the bulging Kevlar walls under wind loading, the uncertainty in the measured material properties due to the use of a linearly elastic model may be over 10% based on measurements of the elastic moduli at different strain states. The material properties of the 120-style, plain-woven Kevlar 49 fibers were determined to be $E_x = 1.33 \times 10^{10}$ Pa, $E_y = 3.12 \times 10^{10}$ Pa, and $\nu_{xy} = 0.40$, assuming an effective thickness of $h = 0.0210$ mm. The x -direction, or streamwise direction, corresponds to what is conventionally referred to as the warp direction of the fabric, and the y -direction, or spanwise direction, corresponds to the weft direction of the fabric, these two directions running perpendicular to each other in the undeformed state.

It is noted that the Kevlar walls of the wind tunnel for this study were painted with a randomized speckle pattern of screen printing ink to provide contrast for optical measurements. The effect of the ink on the material model of the Kevlar is not known precisely; however, the test fabric sample used to determine the material properties quoted above was also painted with a speckle pattern to reproduce the fabric used in the wind tunnel.

2.4 Regularization technique

Due to the inverse nature of the calculations, the displacement inputs to Eq. 8 should be treated to mitigate the effect of measurement noise on the final computed Δp . First, the displacements from the measurement system are projected onto a coarser grid using C^2 continuous triangulation-based bicubic interpolation. Second, the data are regularized by least-squares projecting the data onto basis functions. Since there does not exist exact analytic representations of the geometrically non-linear deflection solution of thin structures, a series of basis functions are used where the accuracy of the solution depends on the number of terms retained in the series. Global polynomials

were selected for the basis functions in this study as shown in the following equation:

$$u = \sum_{i=0}^a \sum_{j=0}^b l_{ij} x^i y^j \quad v = \sum_{i=0}^c \sum_{j=0}^d m_{ij} x^i y^j \quad w = \sum_{i=0}^e \sum_{j=0}^f n_{ij} x^i y^j, \quad (9)$$

where x and y have their origin as described by Fig. 2 and coefficients l_{ij} , m_{ij} , and n_{ij} are determined by least-squares regression with the raw data. The polynomials are here unrestrained at the boundary of the walls, this arrangement being consistent with the small measured deflection of the tension frame under load. The values for the constants a , b , c , d , e , and f are selected through the sensitivity study in Sect. 4.1.

2.5 Fluid control volume analysis

The transverse loading on a model in the test section is calculated from Δp of Eq. 8 using a momentum control volume analysis of the flow between the test section boundaries. The calculations in this article focus on two-dimensional airfoil experiments where the two-dimensional lift coefficient, C_l , is determined from a spanwise-average Δp , the averaging range to be described in Sect. 5.3. Assuming steady-state, incompressible, and two-dimensional flow, Eq. 10 presents in coefficient form the lift force per unit span reacted through the

airfoil as a function of the test section wall pressures and the fluid exchange across all four boundaries in Fig. 2:

$$C_l = \frac{1}{c} \left[\int_{x_1}^{x_2} (C_{p,4} - C_{p,3}) dx + \int_{z_3}^{z_4} \frac{(w_1 u_1 - w_2 u_2)}{\frac{1}{2} V_\infty^2} dz + \int_{x_1}^{x_2} \frac{w_4^2 - w_3^2}{\frac{1}{2} V_\infty^2} dx \right], \quad (10)$$

where c refers to the chord length, u refers to the streamwise velocity component, w refers to the transverse velocity component, the subscripts 1 and 2 refer to values at the entrance and exit to the test section, respectively, and the subscripts 3 and 4 refer to values at the port-side and starboard-side walls, respectively, and where

$$C_p = \frac{p_{\text{chamber}} \pm \Delta p - p_\infty}{\frac{1}{2} \rho_\infty V_\infty^2}. \quad (11)$$

where p_{chamber} is the static pressure in the anechoic chamber adjacent to each respective wall, p_∞ is the freestream static pressure, ρ_∞ is the freestream air density, V_∞ is the freestream velocity, Δp is the wall pressure difference of Eq. 8 calculated using the coordinate system described in Fig. 2, and the sign before the Δp term depends on which wall is being considered (the positive is taken for the starboard wall and the negative for the port wall). Regarding the small-angle approximation stemming from Eq. 7 and also implicit in Eq. 10, the angle of deflection of the Kevlar in both azimuth and inclination should remain small which will be confirmed in Sect. 5.3.

The relative magnitudes of each of the terms in Eq. 10 are discussed in Brown (2016) where it is noted that the first term is by far dominant. The second term amounts to a correction for the small transverse momentum flux entering and exiting the test section undetected by the wall pressure measurements which have only finite length in the streamwise direction. Using calculations similar to those of Von Doenhoff and Abbott (1947), this second term amounts to an increase in C_l of 2.5 and 6.1%, respectively, for the 4.7 and 3.6-m streamwise extents of the pressure measurements to be referenced further below. The third term accounts for the momentum flux through the porous walls which affects C_l by less than 0.5% for all cases considered in this study. The calculations in this paper account for the first and second terms while neglecting the third term.

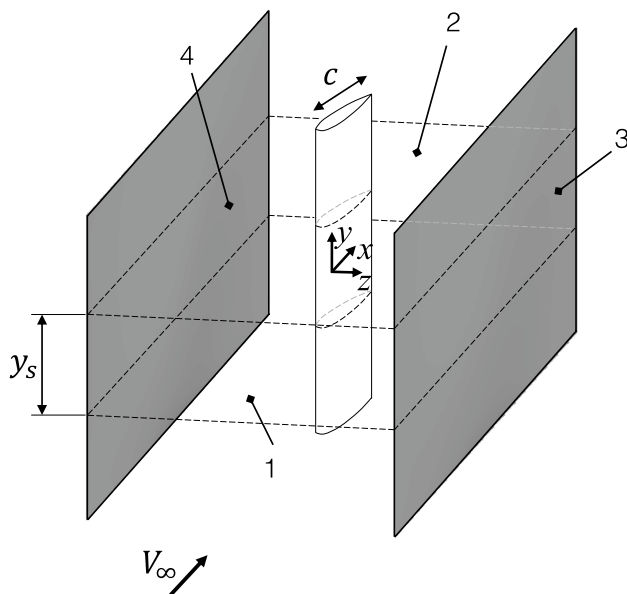


Fig. 2 Schematic illustrating the control volume region of the Kevlar-wall test section. The origin of the coordinate system is centered on the midspan of the test section and the quarter-chord location of the airfoil model. Positive lift is in the positive z -direction, and the spanwise averaging region is given by y_s

2.6 Solution approach

The inverse pressure calculations and subsequent lift integration in this article are based on measured, three-component wall displacements which are then fit to the basis functions in Eq. 9. The differentiated basis functions are then input into Eq. 8, along with the Kevlar material properties and pre-tension distributions derived from auxiliary measurements. Equation 8 allows direct calculation of Δp at each location along the Kevlar, and simple measurement of the static pressure in the anechoic chamber on the back side of the Kevlar then provides the absolute pressure on the Kevlar wall's internal surface. The wall pressures are used to calculate the C_l of the model from Eqs. 10 and 11 which are then validated against reference values of C_l from two other independent measurement techniques.

3 Experimental methods

This section outlines the experimental technique of the wind tunnel tests used to validate the proposed measurement technique.

3.1 Wind tunnel facility

The experiments take place in the 1.85 by 1.85-m Stability Wind Tunnel at Virginia Tech which is a low-speed, single-return type. The maximum Reynolds number per meter is 5 million, and turbulence intensity levels range between 0.016–0.031%.

The experiments are performed with the wind tunnel in Kevlar-wall configuration as shown in Fig. 3. The Kevlar windows are the test section's most unique feature, extending 4.2-m of the total 7.3-m test section length and spanning from the floor to the ceiling. Each window is formed from a single piece of 120-style fabric composed of plain-woven Kevlar 49 fibers. The floor and ceiling surfaces of the test section are composed of aluminum panels, either perforated plates covered in Kevlar for acoustic purposes or solid plates in the case of those nearest model.

The Kevlar walls are tensioned in both the horizontal and vertical directions with a tensioning frame as shown in the detail view in Fig. 4. Tension is produced by applying torque to rollers on the perimeter of the tension frame, and the Kevlar is held in the rollers by an interference fit between locker rods and grooves in the rollers. In addition to the tensioning

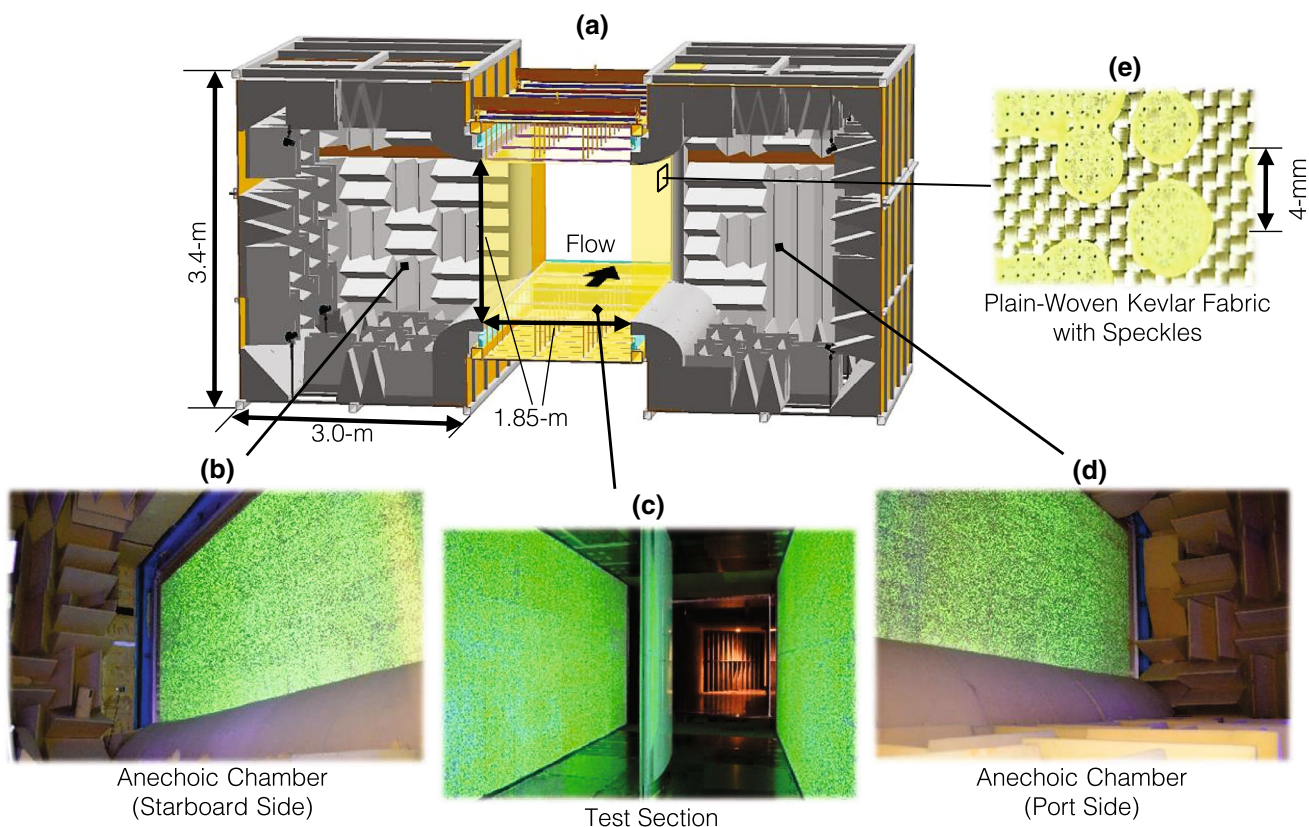


Fig. 3 **a** Downstream-looking rendering of the 1.85-m by 1.85-m Kevlar-wall test section and flanking anechoic chambers. Photos corresponding to the rendering depict the **b** starboard anechoic chamber, **c** the test section with the 0.91-m NACA0012 airfoil, **d** the port anechoic chamber, and **e** a close-up of the speckled Kevlar fabric. The yellow speckles on the Kevlar walls take on a green hue under UV illumination

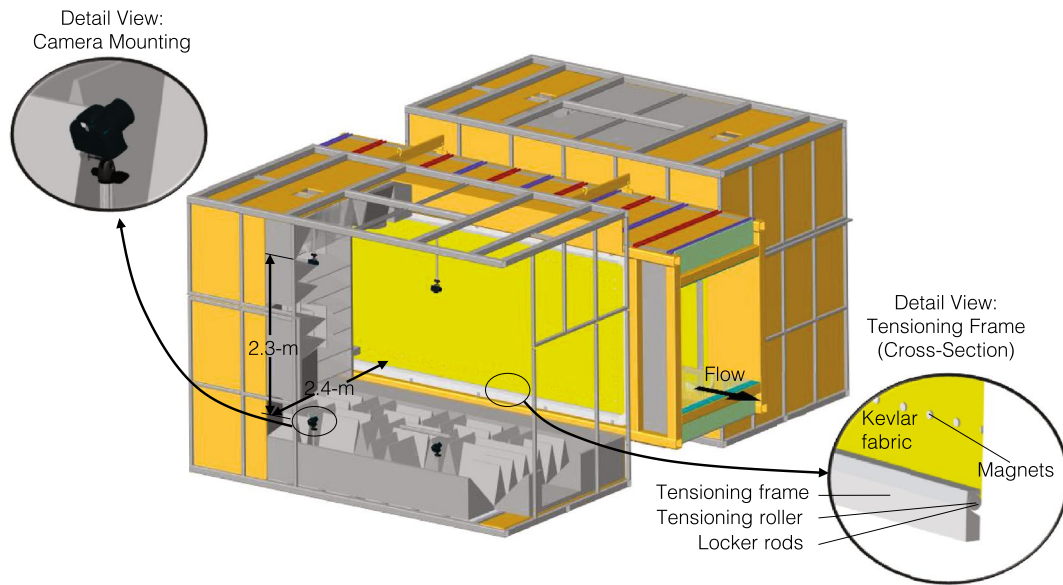


Fig. 4 Cut-away rendering of the port-side Kevlar wall and anechoic chamber

rollers, magnets are spaced roughly 12-cm apart around the perimeter of the window opening in an attempt to keep the Kevlar pressed firmly against the test section even under wind loading.

Tension in the Kevlar sheet is measured with a hand-held tension meter which measures the normal force required to deflect the Kevlar by a known distance out-of-plane. The tension meter designed for the tests has a sensing area of 6.0 by 6.4 cm, and its uncertainty was estimated at ± 140 N/m after calibration against a commercial meter which was limited to measuring horizontal surfaces (Brown 2016). Tension measurements were made at 35 points spaced over each of the Kevlar walls, yielding mean Kevlar pre-tensions of $T_{x,0} = 3300$ N/m and $T_{y,0} = 2500$ N/m for the port wall and $T_{x,0} = 4100$ N/m and $T_{y,0} = 3300$ N/m for the starboard wall, these values showing no strong variation with either temperature or duration of the test campaign.

On either side of the test section are anechoic chambers designed to house acoustic instrumentation. The chambers each run 5.6-m long in the streamwise direction, and thus, they are longer than the streamwise length of the Kevlar walls. The chambers are designed to be sealed from the control room, and the static pressure in each chamber is a function of the wind loading placed on its respective wall.

3.2 Airfoil model

The model tested in this experiment is a full-span 0.91-m NACA0012 airfoil constructed of a composite fiberglass exterior enclosing a core of steel ribs and polyurethane foam (Brown 2014). Tubular quarter-chord spars on either end of the model are rotated through angles of attack by a bearing

and turntable system situated just outside the test section, and the angle of attack is measured with a laser depth-finding reading taken near the trailing edge (Kuester et al. 2015). Mylar strips cover any spanwise gap between the model and the floor/ceiling. Near the midspan, 81 pressure taps of 0.5-mm diameter are spaced around the profile.

3.3 Conventional pressure measurements

The pressure taps in the airfoil are connected to 1.6-mm Tygon tubing which leads to an Esterline 9816/98RK pressure scanner with a range of ± 2.5 psi, accuracy of $\pm 0.05\%$ full scale (which accounts for hysteresis, non-linearity, and non-repeatability), or ± 9 Pa, and resolution of $\pm 0.003\%$ full scale, or ± 0.5 Pa. The pressures are integrated along the airfoil surface to yield lift and/or pitching moment.

Temporary pressure taps are additionally installed in the Kevlar walls to measure the midspan pressure distribution over the walls. There are 30 taps per wall, and the spacing between taps varies from 10.2 cm (4 in.) to 20.3 cm (8 in.) for a total streamwise coverage of 4.7 m (184 in.). The pressure taps are made by sanding off one side of a polypropylene connector designed to accept 1.6 mm (1/16 in.) inner diameter tubing. The connector and its attached Tygon tubing are then hot-glued to the chamber side of the Kevlar wall. The tubing runs down the wall and to an Esterline 9816/98RK pressure scanner with a range of ± 10 inches of water. The static pressure generated in the anechoic chambers is also measured with the Esterline scanner.

3.4 Wall deformation measurements

Inverse measurement of the wall pressure field hinges upon accurate measurement of wall deformation. Building upon the previous work to measure the wall deformations (Ito et al. 2010), the current measurement system employs three-dimensional digital image correlation (3D-DIC) techniques to measure the full-field deformation of the Kevlar walls.

The layout for the 3D-DIC system includes cameras mounted in each anechoic chamber and directed at the Kevlar walls, as shown in Fig. 4. Each anechoic chamber has two pairs of stereo cameras, an upstream and downstream pair, which together capture a 3.6-m streamwise extent and nearly the full 1.85-m height of the Kevlar walls. The stereo angle between pairs is 42° in accordance with best practices for measurements featuring relatively large out-of-plane deformation magnitudes (Sutton et al. 2009). The cameras are placed at 2.4-m depth from the Kevlar-walls and at the largest baseline separation afforded by the anechoic chambers of 2.3 m. Focal lengths of 21 to 24 mm are chosen to allow for some overlap of the field-of-view between the upstream and downstream pairs of cameras. Given the above camera layout and an aperture of $f/18$, the lenses are focused well beyond their hyperfocal lengths, and the Kevlar walls remain within the depth-of-field of the lenses even as the walls deflect inwards and outwards under wind loading.

The cameras themselves are Canon Rebel T3's which are digital single-lens reflex (DSLR) type. Each camera has a 4272 by 2848 pixel CMOS sensor with 5.2- μm square pixels and 14-bit dynamic range. The cameras are fitted with EF-S 18–55 mm 1:3.5–5.6 IS II lenses from Canon. Each camera/lens pair is mounted to a Manfrotto 808RC4 camera mount which is then bolted to an aluminum support affixed to the super structure of the anechoic chamber, as shown in Fig. 4.

Remote image capture is performed at an exposure of 8 s with an ISO of 100. The long exposure time permits a smaller aperture and is acceptable since motion of the Kevlar walls is not a concern during testing of steady flows. When flow separation over a model becomes prevalent at extreme angles of attack, the walls experience buffeting which correlates with the shedding of vorticity from the model. For these limited cases, a faster exposure time would, indeed, be optimal to minimize blur from unsteady wall fluctuations but is not pursued in this article. As a result, there is higher uncertainty associated with the wall deformation measurements when there is flow separation over the model.

Images are converted from raw to bitmap format before being imported to DaVis 8.2.3 software from LaVision. Pre-processing in the software includes defining the zero planes for each Kevlar wall using measurements of the unloaded walls, as well as calibrating each of the four stereo camera systems. A planar auto-calibration via the bundle adjustment

method was performed using five to six images for each stereo-pair (Zhang 1999).

Estimates of residual uncertainty due to calibration error and feature-matching error were derived from measurements of a printed speckle pattern that was placed just in front of the Kevlar walls and affixed to a translation stage with 10- μm resolution. The in-plane uncertainty was thus estimated at $\pm 40\text{-}\mu\text{m}$ for 20:1 odds, and the out-of-plane uncertainty at $\pm 60\text{-}\mu\text{m}$. Errors did not stack up across sequential measurements, since each new deformation image during an angle of attack sweep was calculated relative to the undeformed state.

An additional source of uncertainty not accounted for in the uncertainty estimates just described is due to sub-millimeter deformation of the pressurized anechoic chambers to which the cameras were mounted during testing which caused slight movement of the cameras. This uncertainty turned out to be significant for some cases, especially those tests involving high freestream dynamic pressures. A correction procedure which aligned displacements between the upstream and downstream stereo-pairs worked to minimize the uncertainty but added a rigid-body translation uncertainty of roughly 0.5 mm to the absolute displacements, as well as uncertainty due to rigid-body rotation between stereo-pairs which was small but likely significant. In total, the achieved displacement uncertainty is significantly larger than the $\pm 40\text{--}60\text{-}\mu\text{m}$ values quoted above though not quantified precisely. The uncertainty is least at low freestream dynamic pressures which is the focus of this article.

To produce the high-contrast, random patterning necessary for DIC algorithms, the Kevlar walls are marked with circular paint specks that are randomized in both location and size. There are on average 3.5 speckles per cm^2 which produce 31% coverage of the Kevlar's surface area. The pattern is produced by applying fluorescent ink to a patterned, linoleum screen-printing block and pressing the block against the tensioned Kevlar sheet. The speckles are illuminated with UV light during measurements, as shown in Fig. 3 to provide high optical contrast which aids the DIC algorithm accuracy. No measurements have yet been made to quantify the effect of the speckles on the acoustic transmission of the Kevlar walls, though the bulk cross-flow through the Kevlar pores for a given pressure difference is reduced by $\sim 9\%$ (Brown 2016). The effect of the speckles on the material model of the Kevlar was referenced in Sect. 2.3.

The DIC calculations use second-order polynomials for the shape function, and sub-pixel interpolation is accomplished with sixth-order splines. Processing proceeds with a square window size 61 by 61 pixels with each speckle occupying at least 3 by 3 pixels. The resulting spatial resolution is 1.6 cm in both directions for a total of 34,000 measurement locations per Kevlar wall. These data are first projected onto a grid of cell size 4 by 4 cm (120 by 46 nodes) before being additionally regularized by projection onto Eq. 9.

4 Sensitivity analyses

This section quantitatively assesses the sensitivity of the inverse calculation methodology with respect to measurement noise and regularization approach, as well as with respect to the uncertainty in the fabric properties. The analyses employ finite-element simulations of which the mesh convergence and verification are demonstrated in Brown (2016). The simulations are performed in MSC-Nastran with four-noded shell elements which are both materially linear and orthotropic. The analysis is geometrically non-linear which includes both element coordinate update and follower forces.

A rectangular membrane with the same 5.14 by 1.85-m Kevlar region as the wind tunnel walls is fixed in all six degrees of freedom at the boundaries and divided into a mesh of 344 by 124 elements, thus closely replicating the spatial resolution of the 3D-DIC measurements which is 1.6 cm in both directions. Uniform pre-tension of 3300 N/m in both x - and y -directions is developed with thermal loading of elements, and uniform pressure loading of 154 Pa is applied across the membrane as a simplified representation of the wall loading of the experiments to be presented below. The 154-Pa loading, which equates to 0.2 times the freestream dynamic pressure, q_∞ , of the wind tunnel experiments, represents the mean absolute Δp experienced by the tunnel walls operating at the given q_∞ . The mean loading estimation is based on the wind tunnel measurements from the midspan reference taps on the suction-side wall at $C_{l,\max}$ during the present experiment, and thus, the mean loading represents an upper bound to that which is experienced by the Kevlar walls in this paper. Though the mean loading of the simulation matches that of the wind tunnel experiments, the distributions of loading from the experiments are not replicated which should be borne in mind when interpreting the simulation results in this section. The material properties of the simulated Kevlar are the same as those reported in Sect. 2.3 with the exception of G which cannot be zero for numerical reasons and is set to between $1e3$ and $1e6$ Pa.

To evaluate different regularization techniques in the presence of noise, it is necessary to interpolate the raw finite-element results to grids of different coarseness as will be done below. Such interpolations are accomplished with bicubic interpolation.

4.1 Sensitivity to measurement noise

To judge the efficacy of the regularization approach described in Sect. 2.4, Gaussian noise of the same magnitude estimated previously for the experimentally measured displacements is added to each component of the simulated

displacements. The first step in the regularization approach is interpolation of the noisy data onto a grid of element size 4 by 4 cm using C^2 continuous triangulation-based bicubic interpolation. Comparing the interpolated values to the similarly interpolated un-noised data, the residuals show random scatter in space with uncertainties across the sheet of less than $33\text{ }\mu\text{m}$ for the u displacements, $33\text{ }\mu\text{m}$ for the v displacements, and $48\text{ }\mu\text{m}$ for the w displacements, as compared to the input noise levels of 40, 40, and $60\text{ }\mu\text{m}$, respectively, at 20:1 odds. The second step in the regularization process is the polynomial fitting process which, when using the optimally determined number of polynomial terms as shown below, further reduces the uncertainty to under $12\text{ }\mu\text{m}$ for the u displacements, $5\text{ }\mu\text{m}$ for the v displacements, and $9\text{ }\mu\text{m}$ for the w displacements.

To determine the optimal number of polynomial terms to include in the regression, it is specified that $A \equiv a = c = e$ and $B \equiv b = d = f$ in Eq. 9. Such an arrangement corresponds to holding the order of the polynomials for the u , v , and w displacements the same in each respective coordinate direction. Both even and odd orders of polynomial terms are included since the experimental implementation of this method will invariably have asymmetries present. Using simulation results with added noise, the best-fit coefficients of the even terms are generally several orders of magnitude greater than those of the odd terms.

Proceeding with the sensitivity study, the values of A and B are each parametrically varied from 2 to 12 in a nested loop, and analytic derivatives of the fitted displacements are evaluated in Eq. 8. The difference between the inverse calculation, Δp , and the actual uniform pressure field enforced by the finite-element simulation, Δp_e , is then sampled between the limits of $x = \pm 2.0\text{ m}$ and $y = \pm 0.65\text{ m}$ to determine which parametric variation has the lowest variance of error.

Figure 5 shows the results of the sensitivity study where subfigure (a) indicates the increase in the order of the optimal polynomial basis functions and corresponding decrease in variance error across the sheet as the level of measurement noise falls. For the measurement noise levels specific to this study, the orders of the highest terms in the polynomial basis functions are optimally 9 and 6 for the x - and y -directions, respectively, yielding a 20:1 odds uncertainty in Δp across the sheet of 0.001 times the specified q_∞ . For the distribution of the residuals in Fig. 5b, there is some periodicity to the residuals which suggests that there is yet room for improvement in the formulation of the basis functions, though the bias pattern is not strong.

The above-calculated uncertainty in Δp of $0.001 \times q_\infty$, or 0.7-Pa, is indeed on par and in most cases better than that of the pressure transducers typically used in low-speed wind tunnel applications. This accuracy is a best-case value, however, since the actual experimental implementation of

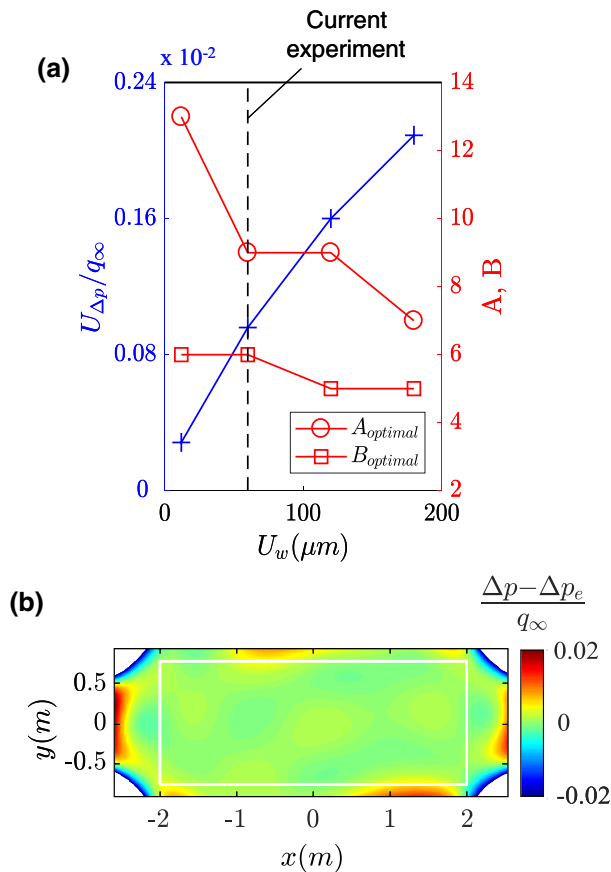


Fig. 5 **a** Sensitivity of the normalized uncertainty in Δp , $U_{\Delta p}/q_{\infty}$, and of the optimal polynomial fitting parameters, A and B , to the uncertainty of the simulated displacement inputs with added noise, U_w . Noise levels applied to the u - and v -components are two-thirds those shown for U_w , and all uncertainties are given at 20:1 odds. **b** Distribution of error between the inversely calculated pressure, Δp , and the enforced pressure, Δp_e , over the Kevlar sheet for the optimal case of $A = 9$ and $B = 6$. The white box indicates the region inside which $U_{\Delta p}/q_{\infty}$ is calculated

the inverse calculation will include additional uncertainties due to the fabric properties as examined below.

4.2 Sensitivity to fabric properties

The sensitivity analysis is now extended to consider uncertainties in the measurements of material properties and pre-tensions of the Kevlar sheet. Using un-noised finite-element results, partial derivatives of Δp from Eq. 8 are calculated at the center-point of the Kevlar wall with respect to the five input parameters E_x , E_y , ν_{xy} , $T_{x,0}$, $T_{y,0}$. If the propagated error in Δp from each of these inputs is restricted to $0.002 \times q_{\infty}$ and assuming that each of the errors is random and uncorrelated, then the combined error in quadrature due to all five parameters will not exceed a level of $0.005 \times q_{\infty}$ which is a typical accuracy for a

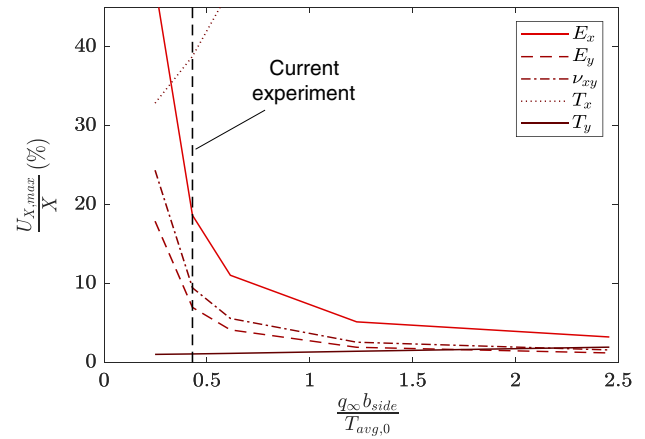


Fig. 6 **a** Maximum allowable uncertainty as a percent of nominal value, $\frac{U_X}{X}$, for each of the five listed input parameters in order to limit error contributions to Δp to $0.002 \times q_{\infty}$ per parameter as calculated at the center-point of the Kevlar wall. The horizontal axis plots freestream dynamic pressure, q_{∞} , non-dimensionalized on the average pre-tension in the Kevlar sheet, $T_{avg,0}$, and the shorter side length of the Kevlar sheet, b_{side}

pressure reading in low-speed wind tunnels. To the accuracy of the linearized partial derivatives, the maximum allowable uncertainty for each input parameter is thus the quotient of the maximum allowable uncertainty in Δp divided by each partial derivative as given by the following equation:

$$U_{X,max} = \frac{0.002 \times q_{\infty}}{\partial \Delta p / \partial X}, \quad (12)$$

where U is the maximum uncertainty permitted in the nominal value of any one of the five input parameters denoted as X .

The $U_{X,max}$ as a percent of X are plotted in Fig. 6 versus q_{∞} which has been non-dimensionalized on the ratio of average tension in the Kevlar sheet, $T_{avg,0}$, to the shorter side length of the Kevlar sheet, b_{side} . For lower values of $q_{\infty} b_{side}/T_{avg,0}$, the membrane problem tends towards geometric linearity, and thus, the required accuracy of the pre-tension inputs is most stringent. On the other hand, as the value of $q_{\infty} b_{side}/T_{avg,0}$ increases, the problem becomes fully non-linear in the geometric sense which then requires higher accuracy for the material properties inputs.

For the value of $q_{\infty} b_{side}/T_{avg,0}$ to be examined in this study, $T_{y,0}$ is the most restrictive input and should be known to within 1% which is comparable though more stringent than afforded by the tension meter described in Sect. 3.1. Considering both the meter's quoted uncertainty and the measured $T_{y,0}$ values of the wind tunnel walls, the meter should achieve accuracy of ± 4 –6% of $T_{y,0}$. Setting Eq. 12 equal to the actual uncertainty of the tension meter and recalculating the results, the expected error due to the $T_{y,0}$

measurement is thus around $0.009 \times q_\infty$ and is, therefore, the dominant uncertainty in the Δp calculation. On the other hand, the value of $T_{x,0}$ need not be known with better than 30% uncertainty which follows since the aspect ratio of the Kevlar wall is 2.9 times longer in the x - than the y -direction, thus producing significantly lower $\partial^2 w / \partial x^2$ than $\partial^2 w / \partial y^2$. This state of events is also evident in the more stringent requirements on the accuracy of E_y than E_x in Fig. 6, though the required accuracy of the E_x , E_y , and v_{xy} terms is already on the same order as the estimated uncertainties of these quantities as noted in Sect. 2.3.

5 Results

Measurements on the 0.91-m NACA0012 airfoil were performed without forced transition of the boundary layer and at q_∞ of 770-Pa, corresponding to $Re = 2.0e6$ and $Ma = 0.11$. The airfoil C_p distribution and wall C_p distribution were measured over angles of attack from 0 to 18° . All angles of attack, pressures, and lift coefficients are reported without correction for wall interference.

5.1 Measurement of Wall Displacement

This section presents the global wall displacement fields and displacement derivatives under wind loading used to inversely calculate wall C_p distributions. The three-component displacement contours for a geometric angle of attack of 7.8° are shown in raw form in Fig. 7. The distribution of the w -displacement data is well behaved and generally symmetric, the largest displacement occurring near the center point of the wall. The distributions of the in-plane u and v displacements, which are notably two orders of magnitude less than the w displacements, have less intuitive yet still physical features. The v displacements near the airfoil show the fabric displacing away from the origin as a result of the tilting pressure vector. Near extreme y values, the direction of the v displacement reverses because the longer sides of the roller frame are bowing inwards under the tension of the fabric. The u displacements indicate that the fabric is pulling inwards towards the origin on the upstream side, suggesting that the shorter sides of the roller frame are also bowing slightly under the tension of the fabric. The u displacements also contain artifacts of the wall-mounted reference pressure taps as shown by the vertically running bands in Fig. 7a. Though the induced error of these artifacts is believed small due to the fact that the number of periodic bands is more than three times the highest order of the fitting polynomials, the induced error of these artifacts should be borne in mind when interpreting the results below.

Using the regularization process described in Sect. 2.4 and the optimal order of polynomials described in Sect. 4.1,

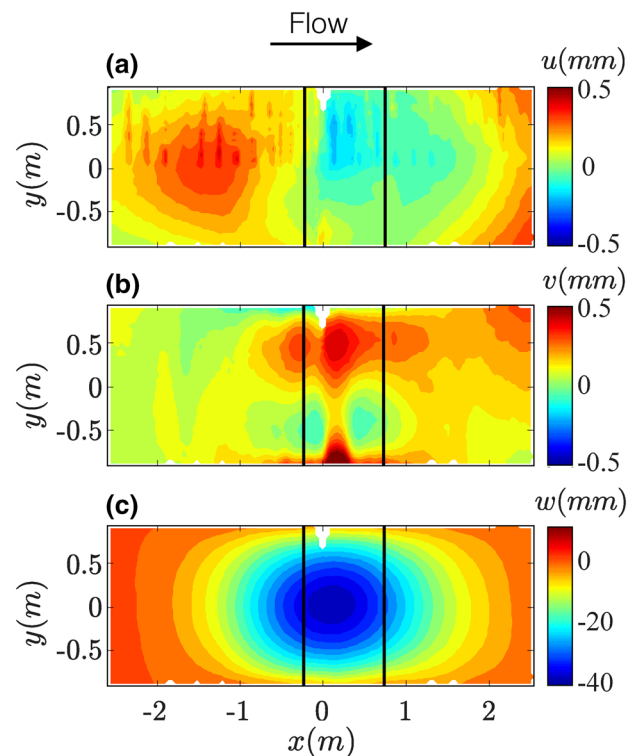


Fig. 7 Raw displacements on the suction-side Kevlar wall at geometric angle of attack of 7.8° . The vertical black lines show the projection of the airfoil

the typical coefficients of determination (R^2) values for the polynomial fits were 0.95, 0.80, and 1.00 for the u -, v -, and w -displacement components, respectively, where a value of unity indicates a fit with zero residual. The former two values are somewhat less than unity due to the residual misalignment of the stereo cameras as a result of the unintended motion of the cameras described previously, this misalignment creating proportionately greater error in the in-plane components which have significantly smaller magnitude than the out-of-plane component. The final result of the two-step regularization process is that the regularized data retain the character of the raw data but smooth out fluctuations.

5.2 Calculation of wall pressure distribution

The regularized version of the data in Fig. 7 is used to compute each of the non-shear terms of Eq. 7, which along with the pre-tension data are used to calculate C_p values from Eq. 11. All these data are plotted side-by-side in Fig. 8. The distribution of the pre-tensions in Fig. 8a, b includes high corner tension, as well as lower tension along the long sides of the frame, both of which at least partially stem from bowing of the longer lengths of the roller frame. In general, the T_0 magnitudes are larger than the T_ϵ magnitudes for the current experimental conditions, so we may expect

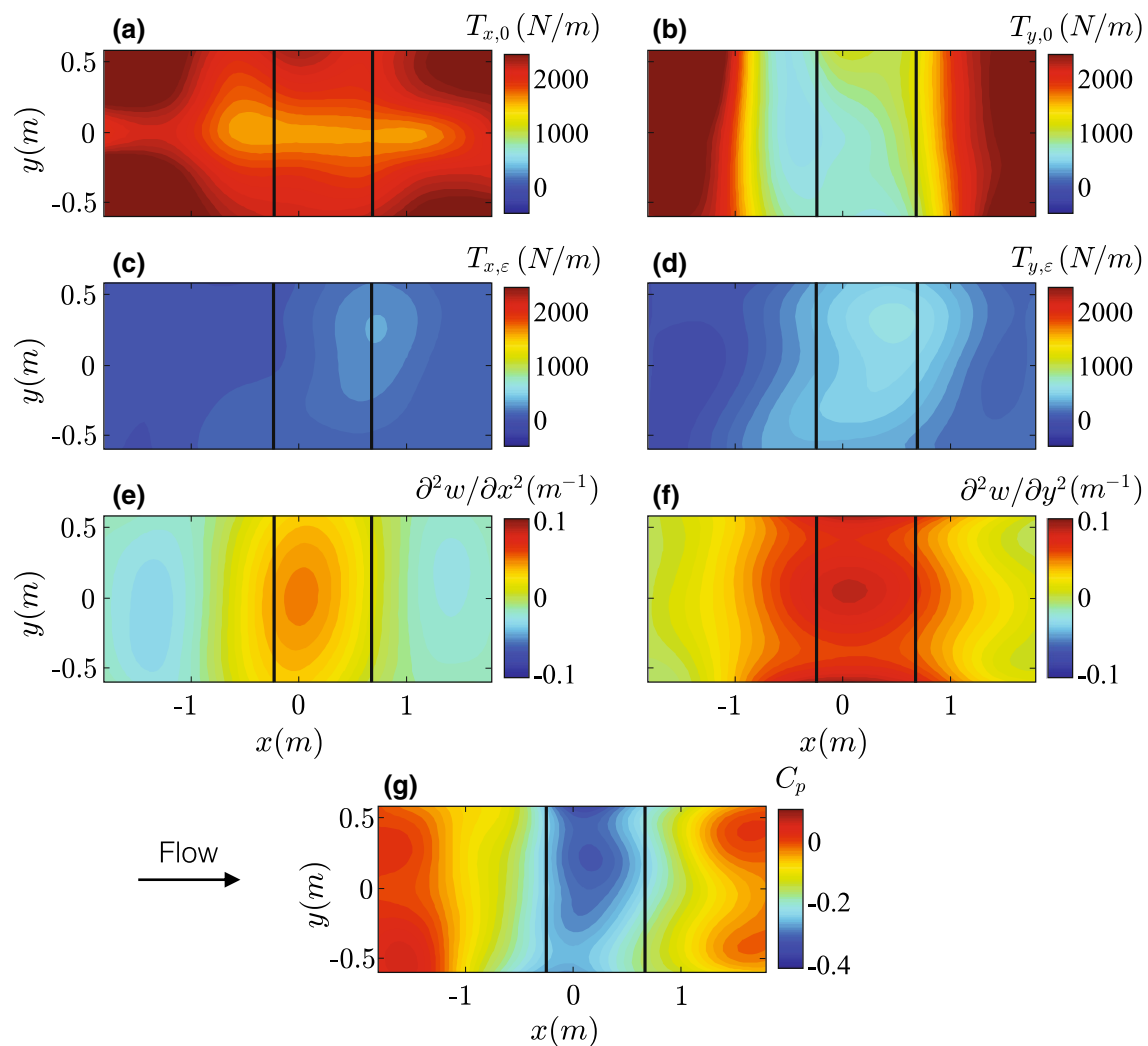


Fig. 8 Data from the suction-side wall at geometric angle of attack of 7.8° . The vertical black lines show the projection of the airfoil

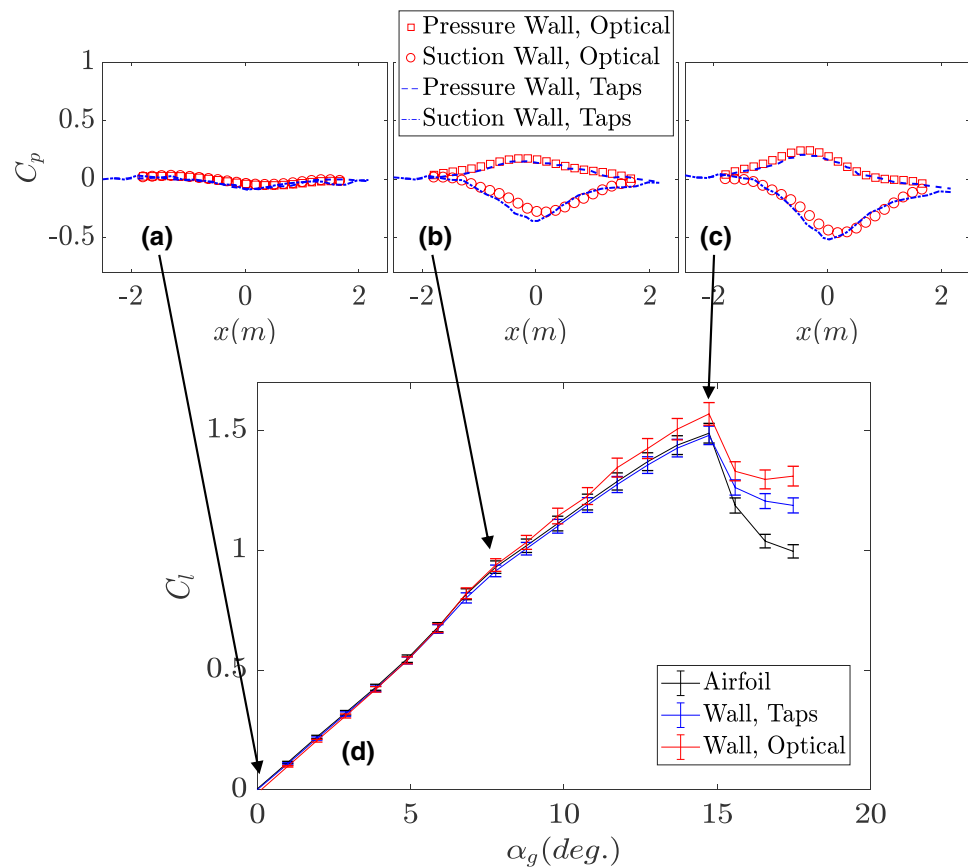
to find smaller though not necessarily negligible contributions to the overall error from the latter. In Fig. 8c, d, the maximum T_ε is shifted away from the line $y=0$ which is plausibly a result of uncertainties in the Kevlar's material properties combined with subtle T_0 -induced asymmetry in the measured deflections. On the other hand, the contour shapes of $\partial^2 w / \partial x^2$ and $\partial^2 w / \partial y^2$ in Fig. 8e, f have peaks of curvature near the origin which correspond to the peak of w displacement in Fig. 7c. In the combined result of the C_p data in Fig. 8g, the minimum C_p peak is again shifted towards the positive y -direction which may be an influence of the asymmetry in the T_ε fields as described. The spanwise non-uniformity of the C_p distribution, which could also stem from over-fitting by the global polynomials, should be borne in mind while interpreting the results below. The C_p contours are otherwise smoothly varying and have more negative C_p near the model's quarter-chord location as expected for the suction-side wall.

5.3 Validation of wall pressure measurements

We now focus attention only on the data in the midspan region as is conventional for two-dimensional airfoil testing. The midspan C_p at any given streamwise location is taken as the spanwise-average of the C_p 's within $y = \pm 0.3$ m of midspan. The midspan C_p measurements are validated against an independent measurement consisting of the midspan wall-mounted pressure taps described previously. The pressure tap measurements were made concurrently to the tests with the optical system.

Figure 9a–c shows the wall C_p distributions for three angles of attack. Note that the C_p 's from the wall-mounted taps have had their empty test section C_p 's subtracted from them to account for imperfect flow-side facing quality of the taps, but no corresponding process has been applied for the optical data as datum subtraction is implicit in the fully non-contact measurement. Both pressure measurement

Fig. 9 **a–c** Optically inferred C_p distributions across the Kevlar walls and **d** integrated C_l values versus geometric angle of attack, α_g , as compared with reference measurements including wall-mounted pressure taps and airfoil surface pressure taps. The data in **a–c** are at α_g of 0, 7.8, and 14.7°, respectively



techniques yield the same overall C_p shape yet with some finer differences apparent including an offset of the suction peak of the optical data relative to that of the wall-mounted taps in the downstream direction. This offset may be related to the spanwise averaging limits of C_p combined with the presence of some spanwise non-uniformity as noted above, or it could stem from exaggerated contributions of T_ϵ relative to T_0 in Eq. 7 resulting from uncertainty in the material properties of the Kevlar. Within the spanwise averaging region, it is noted that the azimuth and inclination angles of the deflected Kevlar surface never exceed 2.5° for all the data in this paper which verifies the small-angle assumption implicit in Eqs. 7 and 10.

The C_l is calculated from the C_p distributions via Eq. 10 as displayed in Fig. 9d, plotted along with the C_l integrated from the wall-mounted taps and the airfoil taps. The C_l trends are replicated well between the three measurement types, including the gentle tilt in slope of the linear region at roughly 7°. At angles of attack above 11°, the optical data deviates more significantly from the other two data sets which may reflect systematic errors in the measurements of the Kevlar pre-tension and material properties which come into play more strongly as lift and thus wall deflection increase. Both types of wall measurements capture a less severe stall than the airfoil measurements which is a

characteristic difference between wall and airfoil measurements for cases where stall originates near the airfoil taps.

Within the un-stalled data, the maximum difference in C_l between the airfoil pressure taps and the optical method occurs at $C_{l,max}$ and is 0.080, or 5.4%, which is near the limit of the uncertainty bounds calculated by propagating error from uncertainties in the primary measurements (Brown 2016). The uncertainty estimates for all three measurement techniques in Fig. 9d include contributions from measurement error in the freestream dynamic pressure reading, local pressure readings, location of local pressure readings, and model chord length. The uncertainty estimates for the optical method are slightly larger than those for the other two techniques due to larger uncertainties in the local pressure readings as stemming from the previously quoted uncertainties in the Kevlar pre-tension and material properties as they propagate through Eq. 8. The uncertainty in the local pressure readings due to measurement noise in the optically measured wall deflections is not included in the uncertainty calculations due to the estimated low magnitude of this uncertainty as described in Sect. 4.1.

5.4 Extension of measurement technique

Towards extending the optical pressure measurement technique across a range of experimental conditions, experiments were also made for cases with higher q_∞ than the 770-Pa results presented. As q_∞ is increased to levels higher than that plotted in Fig. 9, the C_l of the optical method increases beyond the uncertainty bounds of the airfoil data. According to the findings of Fig. 6, this unrealistic bias in the optical C_l 's might be a result of unmodeled non-linearities in the material properties of the woven Kevlar which affect the calculation more strongly as wall deformation and thus geometric non-linearity increase. Another source of bias error which scales with q_∞ is the noted sub-millimeter deformation of the pressurized anechoic chambers to which the cameras were mounted during testing. This error should be remedied by mounting stereo-pairs of cameras on a single support, as well as by the use of fiducial reference markings to align the coordinate systems of different stereo-pairs in the event of relative motion of the pairs. Finally, as loading on the walls increases beyond that considered in this study, violation of the small-angle approximation stemming from Eq. 7 may require use of an inverse finite-element technique such as those described in Sect. 1.3.

Towards a strategy to compensate for the stringent requirements on the definition of the Kevlar pre-tension, as well as to account for any residual movements of the cameras in the anechoic chambers due to pressure loading, one suggestion for future work is to, in effect, calibrate the Kevlar walls by applying a series of constant pressures to the anechoic chambers and measuring both the sub-millimeter movements of the cameras and the deformations of the Kevlar walls. Given accurate material properties of the Kevlar from independent measurements, such a series of calibrations might prove useful to null unintended camera motions and to infer the Kevlar pre-tension including local irregularities.

6 Conclusions

The thrust of this work has been the development and validation of a novel instrumentation technique for Kevlar-wall test sections. The pressure distributions over the Kevlar walls were inferred based on the global deformation of the walls under wind loading as measured by 3D-digital image correlation. The inputs to the problem include the Kevlar material properties, the pre-tension in the walls, and the gradients of deformation under wind loading. Given the inverse nature of the problem, a finite-element study was used to find appropriate polynomial basis functions to mitigate the effect of measurement noise on the computed loading. The so-called optical method of wall pressure measurement notably

provides full-field C_p distributions across the side walls of the wind tunnel and is shown to calculate C_l as measured over a NACA0012 airfoil to within 5.4% of the value measured with pressure taps on the model. Improvements to the measurement should include high fidelity characterization of the Kevlar fabric's pre-tension and material properties, and the experimental setup should be modified to include rigid mounting between stereo-pairs of cameras, as well as fiducial markings to identify any unintended camera movements.

Acknowledgements Funding for this work was provided by the Stability Wind Tunnel at Virginia Tech. The authors would like to thank Dr. Rakesh Kapania and Dr. Robert Canfield for their valuable insights on inverse techniques and membrane mechanics. Dr. Aurelien Borgoltz also contributed meaningful knowledge both to the content in this article and to the preceding development of Kevlar-wall measurement techniques. Bill Oetjens and Tim Meyers of the Stability Wind Tunnel assisted greatly with the experiment. In addition, Julio Estrella and Stephanie Hoang are gratefully acknowledged for their measurements of the Kevlar pre-tension.

References

- Ashill P, Keating R (1988) Calculation of tunnel wall interference from wall-pressure measurements. *Aeronaut J* 92(911):36–53. <https://doi.org/10.1017/S0001924000021813>
- Ashill P, Hackett J, Mokry M, Steinle F (1998) Boundary measurements methods (Chapter 4). *Wind Tunnel Wall Corrections (la Correction des effets de paroi en soufflerie)*, Advisory Group for Aerospace Research & Development (AGARD), NATO, AG-336
- Beccarelli P (2015) *Biaxial testing for fabrics and foils: optimizing devices and procedures*. Springer, Cham
- Brown KA (2014) A study of aerodynamics in Kevlar-Wall test sections, Master's thesis, Virginia Tech, <http://hdl.handle.net/10919/49383>
- Brown K, Devenport W, Borgoltz A, Ura H, Yamamoto K (2014) Towards interference corrections for three-dimensional models in Kevlar-walled anechoic test sections. In: 52nd AIAA aerospace sciences meeting (AIAA 2014-0618), <https://doi.org/10.2514/6.2014-0618>
- Brown KA (2016) Understanding and exploiting wind tunnels with porous flexible walls for aerodynamic measurement, Ph.D. thesis, Virginia Tech, <http://hdl.handle.net/10919/73363>
- Carpenter TJ, Albertani R (2013) Aerodynamic load estimation: pressure distribution from virtual strain sensors for a pliant membrane wing. In: 54th AIAA/ASME/ASCE/AHS/ASC structures, structural dynamics, and materials conference (AIAA 2013-1917), <https://doi.org/10.2514/6.2013-1917>
- Chung PW, Tamma KK (1999) Woven fabric composites developments in engineering bounds, homogenization and applications. *Int J Numer Methods Eng* 45(12):1757–1790. [https://doi.org/10.1002/\(SICI\)1097-0207\(19990830\)45:12<1757::AID-NME653>3.0.CO;2-O](https://doi.org/10.1002/(SICI)1097-0207(19990830)45:12<1757::AID-NME653>3.0.CO;2-O)
- Devenport WJ, Burdisso RA, Borgoltz A, Ravetta PA, Barone MF, Brown KA, Morton MA (2013) The Kevlar-walled anechoic wind tunnel. *J Sound Vib* 332(17):3971–3991. <https://doi.org/10.1016/j.jsv.2013.02.043>
- Devenport WJ, Burdisso RA, Borgoltz A, Ravetta P, Barone MF (2010) Aerodynamic and acoustic corrections for a Kevlar-walled

- anechoic wind tunnel. In: 16th AIAA/CEAS aeroacoustics conference (AIAA 2010-3749). <https://doi.org/10.2514/6.2010-3749>
- Dong Z, Manimala J, Sun C (2010) Mechanical behavior of silica nanoparticle-impregnated Kevlar fabrics. *J Mech Mater Struct* 5(4):529–548. <https://doi.org/10.2140/jomms.2010.5.529>
- Engl H, Kugler P (2005) Nonlinear inverse problems: theoretical aspects and some industrial applications. In: Capasso V, Périaux J (eds) *Multidisciplinary methods for analysis optimization and control complex systems*. Springer, Berlin
- Hearle J, Thwaites J, Amirbayat J (1980) *Mechanics of flexible fiber assemblies*. NATO ASI Series, The Netherlands
- Ito T, Ura H, Nakakita K, Yokokawa Y, Ng W, Burdisso R, Iwasaki A, Fujita T, Ando N, Shimada N, et al. (2010) Aerodynamic/aeroacoustic testing in anechoic closed test sections of low-speed wind tunnels. In: 16th AIAA/CEAS aeroacoustics conference (AIAA 2010-3750). <https://doi.org/10.2514/6.2010-3750>
- Joseph LA, Borgoltz A, Devenport W (2016) Infrared thermography for detection of laminar-turbulent transition in low-speed wind tunnel testing. *Exp Fluids* 57(5):77. <https://doi.org/10.1007/s00348-016-2162-4>
- Kilby W (1963) 2-planar stress-strain relationships in woven fabrics. *J Text Inst Trans* 54(1):T9–T27. <https://doi.org/10.1080/194470263086599100>
- Kuester MS, Brown K, Meyers T, Intaratap N, Borgoltz A, Devenport WJ (2015) Wind tunnel testing of airfoils for wind turbine applications. *Wind Eng* 39(6):651–660. <https://doi.org/10.1260/0309-524X.39.6.651>
- Peng X, Cao J (2002) A dual homogenization and finite element approach for material characterization of textile composites. *Compos Part B Eng* 33(1):45–56. [https://doi.org/10.1016/S1359-8368\(01\)00052-X](https://doi.org/10.1016/S1359-8368(01)00052-X)
- Remillieux MC, Crede ED, Camargo HE, Burdisso RA, Devenport WJ, Rasnick M, Van Seeters P, Chou A (2008) Calibration and demonstration of the new Virginia Tech anechoic wind tunnel. In: 14th AIAA/CEAS aeroacoustics conference (AIAA 2008-2911). <https://doi.org/10.2514/6.2008-2911>
- Shkarayev S, Krashanitsa R, Tessler A (2001) An inverse interpolation method utilizing in-flight strain measurements for determining loads and structural response of aerospace vehicles. Tech. rep, association for computing machinery
- Smith BS, Camargo HE, Burdisso RA, Devenport WJ (2005) Development and testing of a novel acoustic wind tunnel concept. In: 11th AIAA/CEAS aeroacoustics conference (AIAA 2005-3053). <https://doi.org/10.2514/6.2005-3053>
- Stanford B, Albertani R, Ifju P (2007) Inverse methods to determine the aerodynamic forces on a membrane wing. In: 48th AIAA/ASME/AHS/ASC structures, structural dynamics, and materials conference (AIAA 2007-1984). <https://doi.org/10.2514/6.2007-1984>
- Stevens KK (1987) Force identification problems—an overview. In: *Proceedings of the 1987 SEM spring conference on experimental mechanics*, pp. 14–19
- Sutton MA, Orteu JJ, Schreier H (2009) *Image correlation for shape, motion and deformation measurements: basic concepts, theory and applications*. Springer, New York. <https://doi.org/10.1007/978-0-387-78747-3>
- Timoshenko S, Goodier J (1970) *Theory of elasticity*. McGraw-Hill, New York
- Vogel CR (2002) *Computational methods for inverse problems*, vol 23. Society for Industrial and Applied Mathematics, Philadelphia
- Von Doenhoff AE, Abbott FT (1947) *The Langley two-dimensional low-turbulence pressure tunnel*. (NASA-TN-1283)
- Zhang Z (1999) Flexible camera calibration by viewing a plane from unknown orientations. *Computer Vision*, 1999. In: *The proceedings of the seventh IEEE international conference on 1 (IEEE)*, pp 666–673. <https://doi.org/10.1109/ICCV.1999.791289>
- Zhu D, Mobasher B, Vaidya A, Rajan SD (2013) Mechanical behaviors of Kevlar 49 fabric subjected to uniaxial, biaxial tension and in-plane large shear deformation. *Compos Sci Technol* 74:121–130. <https://doi.org/10.1016/j.compscitech.2012.10.012>